Independently Polarization Manipulable Liquid-Crystal-Based Reflective Metasurface for 5G Reflectarray and Reconfigurable Intelligent Surface

Hogyeom Kim[ID], *Graduate Student Member, IEEE*, Seongwoog Oh[ID], *Graduate Student Member, IEEE*, Seungwoo Bang[ID], *Graduate Student Member, IEEE*, Hyunjun Yang[ID], *Graduate Student Member, IEEE*, Byeongjin Kim[ID], *Graduate Student Member, IEEE*, and Jungsuek Oh[ID], *Senior Member, IEEE*

Abstract— **This study presents a new class of independently polarization manipulable liquid-crystal (LC)-based reflective metasurface (RMS) antenna. To the best of the authors' knowledge, this study first introduces independent polarization controllability of the LC-based RMS in mmWave. Two LC layers are embedded into the proposed structure for independent manipulation of the polarization. Isolation topologies, such as rectangular patch shape and metal strip ground, are used to enhance polarization purity, achieving compact bias configuration. The independent polarization controllability and antenna performance, such as aperture efficiency, sidelobe level (SSL), and beam coverage, are validated as a reflectarray. The proposed antenna has a maximum aperture efficiency of 22.5% and beam coverage of over 120°. In addition, the proposed metasurface is used to achieve link connectivity as a reconfigurable intelligent surface (RIS) at millimeter-wave (mmWave) 5G. The demonstration confirms a small-aperture RIS concept, considering spillover and taper efficiencies.**

Index Terms— **Liquid crystal, polarization control, reflectarray, reflective metasurface (RMS) antenna, reconfigurable intelligent surface (RIS).**

I. INTRODUCTION

RECENTLY, millimeter-wave (mmWave) 5G communication has been widely used because of its high data rate. mmWave antennas are required to achieve two major characteristics: 1) high gain to overcome the high transmission loss in the channel and 2) beam scanning ability to attain wide beam coverage [1], [2], [3], [4], [5], [6]. Various antenna topologies have been used for this purpose, including phased-array antennas, transmissive metasurfaces (TMs), and reflective metasurface (RMS) antennas [2], [7], [8]. In contrast to the phased-array antenna, where the antenna requires phase shifters in the feeding network to collimate a beam, the metals of the TM and RM are patterned to achieve an adequate phase-shift range to form the beam. These types of TM or RM are called passive metasurfaces. Instead, active metasurfaces use a dc bias circuit to control the phase distribution of the incident wavefront on the aperture of the TM or RM to collimate and steer the radiated beam from the antenna. The replacement of RF phase shifters with dc bias circuits simplifies the feeding network of the antenna and also reduces the parasitic radiation of the feeding network, RF energy loss, and information loss.

Compared with the TM antenna, the RM antenna can hide dc bias circuits beneath the ground of the RM aperture, resulting in further reduced parasitic radiation from dc bias circuits.

Electromagnetically reconfigurable materials or active components, such as liquid crystals (LCs), p-i-n diodes, and varactors, have been adopted in the unit cell design to control the phase shift made by each unit cell of the RM, [8], [9], [10]. Compared with LC-based RM (LCRM), RMS based on other active components has several issues. For example, the p-i-n diode changes between the two states according to the direction of the current flow. Therefore, the phase shift made by p-i-n diodes is discretized, resulting in quantization loss. Varactor-based RMSs are uneconomical because a number of expensive varactors must be integrated. Moreover, the p-i-n diode and varactor have fixed dimensions and must be surface-mounted on the outermost layer of the RM aperture. The former restricts the minimum dimensions of the unit cell, whereas the latter restricts the design freedom of the unit cell. Furthermore, in high-frequency bands, p-i-n diode-based RMSs are exposed to heat because the dc current operating the p-i-n diodes must flow through the thinner bias line as the dimension of the unit cell decreases.

Therefore, LC was chosen as a reconfigurable material in this study. The LC has several advantages. 1) Lower cost compared with other reconfigurable components because when the frequency increases, the antenna aperture decreases, and the amount of required LC decreases. 2) Low heat emission

Fig. 1. Two conceptual applications of the proposed RMS antenna.

Fig. 2. Orientation of molecules in an LC cavity excited using a bias field.

owing to voltage control. 3) The LC-based unit cell can achieve a continuous phase range with low loss [11]. Although commercial LCs have a lower switching speed than other components, many studies on high-speed switching in the order of nanoseconds have been actively investigated [12], [13], [14].

The LCRM radiates scattered waves in the desired direction as the permittivity of the LC changes. The permittivity of the LC is controlled by the magnitude of the dc voltage, as the electric dipoles in the LC are arranged in the direction of the electric field. The phase shift made by the LC-based RM unit cell is continuous because the permittivity of the LC can be continuously attained by continuous voltage control. Therefore, quantization loss can be removed, in contrast to the p-i-n diode-based design. LCRMs have been previously investigated [15], [16]. Conventional LCRMs exhibit low aperture efficiency and high reflection loss because of the lossy nature of LC. In [8], an LCRM unit cell with low reflection loss compared with previous studies was proposed. Based on this novel unit cell, an RA of high aperture efficiency, as well as wide beam coverage, was proposed [11]. Moreover, studies on the independent controllability of incident polarization have not been reported.

Polarization independence has several advantages to the reconfigurable intelligent surface (RIS) structure. 1) Generally, independently polarization-controllable antennas are preferred in base-station applications because they increase the channel capacity and spectral efficiency. 2) A dual-polarized RIS is suitable for practical base stations that use multiple-input and multiple-output technologies.

This study proposes a novel polarization-independent controllable reconfigurable RMS for mmWave 5G communication. The conceptual design of the proposed RMS, which operates as a reflectarray or an RIS structure, is shown in Fig. 1. The proposed design comprises five dielectric layers and two LC layers supported by two dielectric layers
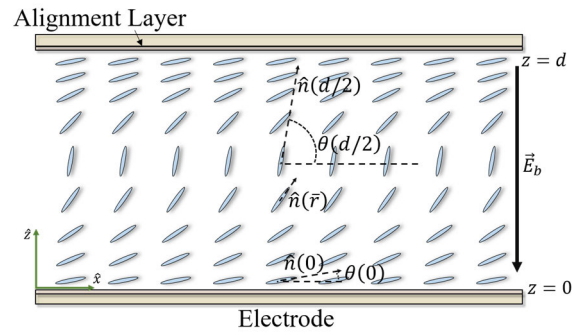
as spacers. Each LC layer is biased by the corresponding controller to control each polarized wave. The measured aperture efficiency and beam coverage of the proposed LCRM are 22.5% and 120°, respectively. In addition, a small-aperture RIS was considered because of the limited biasing capability in the RIS measurement conducted in an anechoic chamber. The small-aperture concept provides some insights. 1) The available power of the RIS cannot be fully defined by the power from the transmitter because the power undergoes spillover and tapers. 2) An electrically large RIS can be seen as a small RIS when the distance between the transmitter and the RIS largely increases. Although path-loss modeling, considering the spillover and taper efficiencies, was introduced in other studies, the demonstration of a small aperture was conducted for the first time in RIS measurement in this article.

The remainder of this article is organized as follows. In Section II, preliminaries on LC basics and the concept of the proposed unit cell are presented. In Section III, a novel unit cell structure capable of polarization-independent phase shifting is examined and the total RMS configuration with the dc bias circuit is examined in detail. In Section IV, the measured results of the reflectarray and the RIS are presented and discussed. Finally, Section V summarizes the results of the study.

II. PRELIMINARIES

A. Principle of Liquid Crystal

The orientation of the molecules in the LC cavity when a bias field excites the cavity is shown in Fig. 2. The bias field induced by an external dc bias voltage forms a quasi-static field. Generally, nematic LCs are used because of their high anisotropy and low loss tangent in the RF band [17]. Molecules of the LC are formed by a rod-like shape oriented in the same direction on average. Consequently, the permittivity of the LC can be macroscopically presented by two values: $\varepsilon_{\parallel}$, in a direction parallel to the principal axis, and $\varepsilon_{\perp}$, in an orthogonal direction. When a zero-bias voltage is applied, the permittivity of the LC is $\varepsilon_{\perp}$, which is the direction defined by the prealigned layer. As the bias voltage increases above the Frederiks threshold voltage V_{th} [18], the orientation direction changes parallel to the principal axis, resulting in permittivity $\varepsilon_{\parallel}$.

As shown in Fig. 2, the permittivity of an LC is represented by a tensor. The relative permittivity tensor is expressed

as follows [19]

$$\overline{\overline{\varepsilon_r}}(\overline{r}) = \varepsilon_{r\perp}\overline{\overline{I}} + \Delta\varepsilon_r\overline{\overline{N}}(\overline{r}) \tag{1}$$

where $\overline{\overline{I}}$ is the second-order identity tensor, $\Delta\varepsilon_r = \varepsilon_\parallel - \varepsilon_\perp$ is the anisotropy of the LC, and $\overline{\overline{N}} = \hat{n}(\overline{r}) \otimes \hat{n}(\overline{r})$ is the second-order tensor. $\hat{n}(\overline{r})$ is a unit vector that is macroscopically defined by the average local direction of the molecules. When the bias voltage is excited, the vector $\hat{n}(\overline{r})$ rotates, resulting in a variation in the permittivity. Notably, the electrostatic energy is converted into elastic energy when the external quasi-static field E_b excites the LC cavity. This energy, called the Frank–Oseen elastic and electrostatic free energy, is minimized such that vector $\hat{n}$ varies.

In extreme states $\varepsilon_\perp$ and $\varepsilon_\parallel$, the permittivity of the LC can be represented by homogeneous permittivity tensors as follows:

$$\overline{\overline{\varepsilon_r}}_\perp \underset{V_b < V_{th}}{=} \begin{pmatrix} \varepsilon_{r\parallel} & 0 & 0 \\ 0 & \varepsilon_{r\perp} & 0 \\ 0 & 0 & \varepsilon_{r\perp} \end{pmatrix} \tag{2}$$

$$\overline{\overline{\varepsilon_r}}_\parallel \underset{V_b \gg V_{th}}{=} \begin{pmatrix} \varepsilon_{r\perp} & 0 & 0 \\ 0 & \varepsilon_{r\perp} & 0 \\ 0 & 0 & \varepsilon_{r\parallel} \end{pmatrix}. \tag{3}$$

This assumes that the alignment layer is rubbed along the x-axis. Although extreme states are associated with the bias voltage V_b, obtaining a representation of the intermediate states between the extreme states is challenging owing to anisotropy and inhomogeneity [19]. However, many studies have defined the intermediate state by homogeneous and isotropic effective permittivity [15], [20], [21].

B. Concept of the Proposed Unit Cell

This section reviews the general form of electric fields used in the following sections. The phase shift of the reflected waves should be manipulated to form a beam reflected by the LCRM, such as collimation, polarization conversion, and wave scattering. Generally, the electric field is expressed as follows:

$$\mathbf{E}^r(\theta, \varphi) = \sum_{n=1}^{N}\sum_{m=1}^{M} \Gamma^{RM}\mathbf{E}^i(\theta, \varphi) \tag{4}$$

where $\mathbf{E}^i = [E_x^i, E_y^i]^T$ and $\mathbf{E}^r = [E_x^r, E_y^r]^T$ represent the two transposed polarized electric field matrices in the incidence and reflection cases, respectively. θ and φ are the elevation and azimuth angles, respectively. In addition, $\Gamma^{\mathbf{RM}}$ can be represented using a 2×2 complex reflection coefficient matrix as follows:

$$\Gamma^{\mathbf{RM}} = \begin{bmatrix} \Gamma_{xx} & \Gamma_{yx} \\ \Gamma_{xy} & \Gamma_{yy} \end{bmatrix}. \tag{5}$$

The coupling coefficient $\Gamma_{xy \text{ or } yx}$ is minimized to independently control the polarization responses. Therefore, $\Gamma_{xy \text{ or } yx}$ is assumed to be zero. In addition, when the permittivity of the LC changes, the corresponding reflection coefficient responds accordingly. This can be accomplished using rectangular patch shapes and a polarizer ground. A detailed explanation of this

phenomenon is provided in the next section. Hence, (5) is replaced by (6) as follows:

$$\Gamma^{\mathbf{RM}} \simeq \begin{bmatrix} \Gamma_{xx}(\varepsilon_{LC1}) & 0 \\ 0 & \Gamma_{yy}(\varepsilon_{LC2}) \end{bmatrix}. \tag{6}$$

The x- or y-polarized incident field $E_{x(y)}^i$ can be expressed as follows:

$$E_{x(y)}^i = Af_{mn}(\theta, \varphi)e^{-jk_0 R_{mn}} \tag{7}$$

where A is the excitation magnitude of the feed antenna. The field pattern of the feed antenna $f_{mm}(\theta, \varphi)$ is modeled with respect to the half-power beamwidth of the feed antenna. In this study, the feed pattern is chosen to be $cos^{11}(\theta)$. k_0 is the free-space wavenumber, and R_{mn} is the distance vector from the feed phase center to any unit cell on the aperture. The complex reflection coefficient of the mnth unit cell was derived using the following:

$$\Gamma_{x(y)}^{RM} = |\Gamma_{x(y)}| f_{mn}^{unit}(\theta_{mn}, \varphi_{mn})e^{j\phi_{mn}} \tag{8}$$

where $|\cdot|$ is the magnitude of the complex vector, and ϕ_{mn} is the phase shift from the mnth unit cell. The field pattern of the unit cell is modeled using $cos(\theta)$. To maximize the reflected field, the unit cell phase shift should satisfy the condition expressed as follows:

$$-k_0 R_{mm} + \phi_{mn} = 2\pi N \tag{9}$$

where N is an integer ($N = 1, 2, 3, \ldots$). This condition is used to collimate the reflected beam.

III. DESIGN OF THE LCRM

This section examines the design of the proposed LCRM, the unit cell design, simulation results, and the entire structure of the proposed LCRM.

A. Design and Principle of the Proposed Unit Cell

An exploded view of the proposed LCRM unit cell (LCRM-UC) is shown in Fig. 3(a). Eight metal and seven dielectric layers were used. The two LC layers were supported by two spacers to create the volume. The relative permittivity of the LC has a complex value ($\varepsilon'_{LC} - j\varepsilon''_{LC}$) owing to its loss feature. The GT7 LC (Merck KGaA, Darmstadt, Germany) was used in this study. Based on the datasheet, the tunable range of the dielectric constant of the LC used in this study is expected to be 2.5–3.5 (from $\varepsilon_{r\perp}$ to $\varepsilon_{r\parallel}$), and the corresponding loss tangent decreases from 0.012 to 0.0064. The real permittivity values of each LC are defined as ε_{1r} and ε_{2r}. The polarizer was modeled as a shunt inductance with respect to the y-polarized waves and a shunt capacitor with respect to the x-polarized waves [22]. Accordingly, the polarizer reflects the y-polarized waves and transmits the x-polarized waves. Therefore, LC2 only influences the x-polarized waves. The geometry of the patches on the upper side of the polarizer was rectangular to reduce the effect of LC1 on the x-polarized waves. As LC2 only influences the x-polarized waves, the metal patch on the top of LC2 is a square shape to distribute the quasi-static electric field into many regions of LC2.
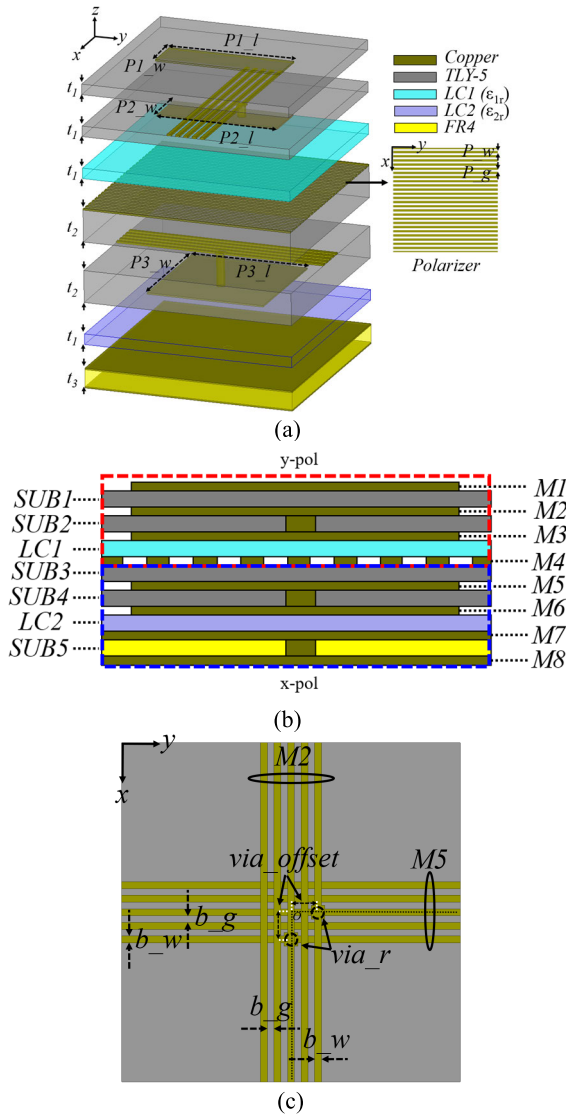
(a)

(b)

(c)

Fig. 3. (a) Exploded view of the proposed LCRM-UC, (b) side view, and (c) bias layers of the top and bottom sides.

TABLE I
GEOMETRIC PARAMETERS OF THE PROPOSED LCRM-UC

Parameter	$P1\_l$	$P1\_w$	$P2\_l$	$P2\_w$
Value	2.7 mm	0.7 mm	2.9 mm	1 mm
Parameter	$P3\_l$	$P3\_w$	P_g	P_w
Value	2.6 mm	2.6 mm	0.1 mm	0.1 mm
Parameter	t_1	t_2	t_3	b_g
Value	0.25 mm	0.76 mm	0.4 mm	0.1 mm
Parameter	b_w	via_r		
Value	0.1 mm	0.2 mm		

are 2.2 and 0.0009, respectively, and those of FR4 are 4.4 and 0.02, respectively. The top view of the two bias layers M2 and M5 is shown in Fig. 3(c).

The bias layer connects metal patches M3 or M6 to the outer control circuit through the via. Each metal patch is connected to the corresponding bias line. The via position changes for each unit cell. The detailed via position layout is presented in the array design section. The via offset ranges from 0 to 0.4 mm with a resolution of 0.2 mm. The geometric parameters of the proposed LCRM-UC are listed in Table I. The periodicity of cells was 5 mm. The thickness of the unit cell is 2.92 mm, and the copper cladding in the unit cell is 1/2 oz. Although the M2 bias layer influenced the x-polarized responses owing to orthogonality, the y-polarized responses were influenced by the via position.

The simulation results for the frequency responses of the magnitude and phase dynamic range versus the extreme bias state are shown in Fig. 4. Extreme phase states associated with the zero-bias state ($\varepsilon_\perp$) and saturation state ($\varepsilon_\parallel$) are represented by solid and dashed lines, respectively. The frequency responses versus ε_{1r} with a fixed ε_{2r} value of 2.5 are shown in Figs. 4(a) and (c), and the frequency responses versus ε_{2r} with a fixed ε_{1r} value of 2.5 are shown in Figs. 4 (b) and (d). The extreme bias states represent the permittivity when zero bias and full bias are applied. The simulation was performed using the commercial software Ansys HFSS full-wave simulator assuming the LC is a homogeneous and isotropic material. The black and red lines represent the magnitude and phase response, respectively.

The y-polarized responses with changing ε_{1r} and ε_{2r} are shown in Figs. 4(a) and (b), respectively. LC1 (ε_{1r}) only influences the y-polarized responses. Owing to M4, the y-polarized responses are only influenced by the top LC (ε_{1r}), where the M4 layer reflects all y-polarized waves. The x-polarized responses with changing ε_{2r} and ε_{1r} are shown in Fig. 4(c) and (d), respectively. Unlike the y-polarized responses, the x-polarized responses were influenced by the top LC owing to the metal layers (M1–3) on the upper side of the polarizer. A rectangular patch shape was introduced in M1 and M3 to reduce the impact on the x-polarized responses. Although the rectangular patch shape has a minor effect on x-polarization, the target frequency experiences a phase shift. The deviation phase shift in the extreme state was 30° at 28 GHz, as shown in Fig 4(d). The maximum reflection loss and phase dynamic range are 4 dB and 260° in the y-polarization cases and 2 dB and 230° in the x-polarization cases, respectively.
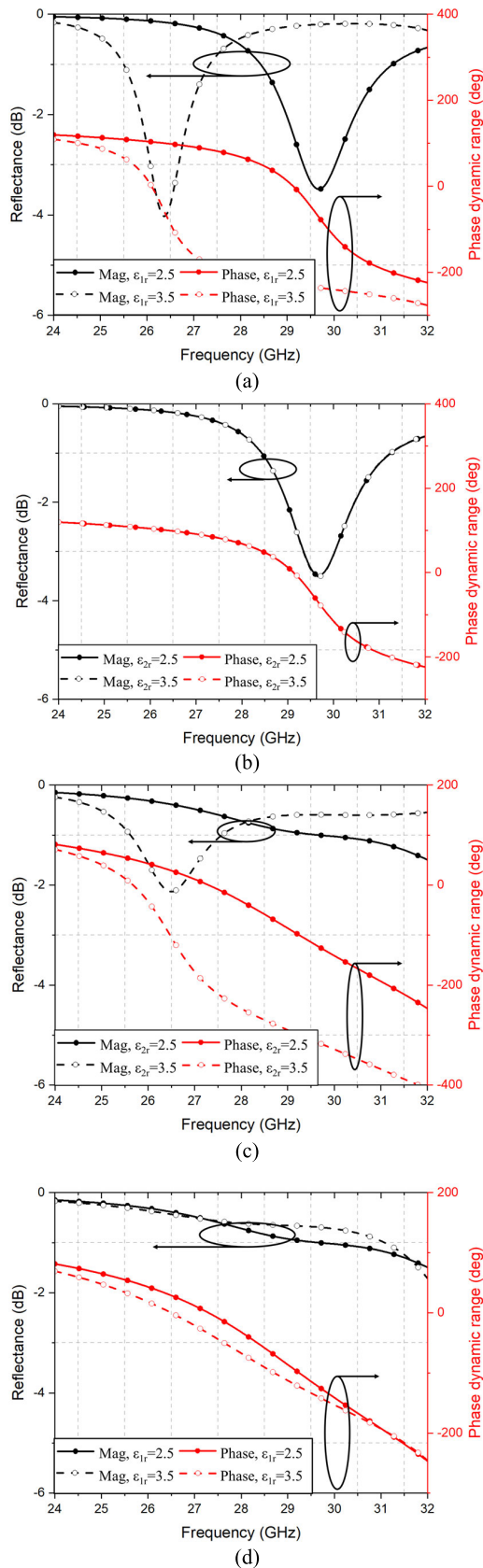
A side view of the proposed unit cell is shown in Fig. 3(b). The dielectric and metal layers in the red box are related to y-polarization. M1 was introduced to achieve low reflection loss related to the y-polarized responses by increasing the thickness of the SUB1 [11]. In addition, bias layers M2 and M5 had deleterious effects on the y- and x-polarization responses. The co-design of the substrate thickness, metal patch size, and bias topology is laborious. The via connects M2 and M3 to the bias-applied voltage from the control circuit. M4 can be modeled as a perfect electric ground with respect to the y-polarized waves. Similarly, the dielectrics and metal layers in the blue box are related to x-polarization. Unlike the case of y-polarization, M4 is modeled as open with respect to the x-polarized waves, which is actually a low-pass filter. A metal via was introduced to connect M5 and M6 to supply a bias voltage to LC2. Taconic TLY-5 was used for the low-loss dielectric from SUB1 to SUB4 and LC spacers. FR4 was selected as SUB5 for the rigid dielectric. The dielectric constant and loss tangent of TLY-5

Fig. 4. Magnitude and phase dynamic frequency responses versus extreme bias states in the case of (a) y-polarized responses with changing ε_{1r}, (b) y-polarized responses with changing ε_{2r}, (c) x-polarized responses with changing ε_{2r}, and (d) x-polarized responses with changing ε_{1r}.

Magnitude frequency responses for each polarization versus the via position from 0 to 0.4 mm are shown in Fig. 5. Unlike
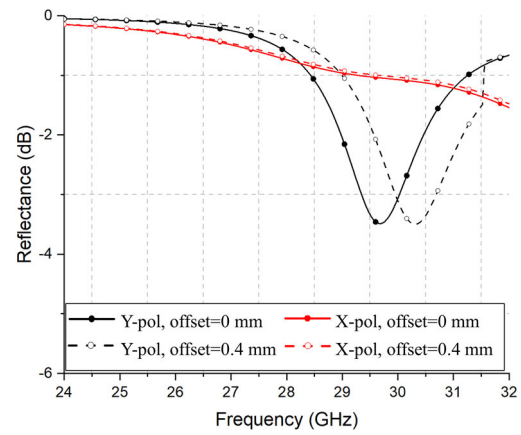

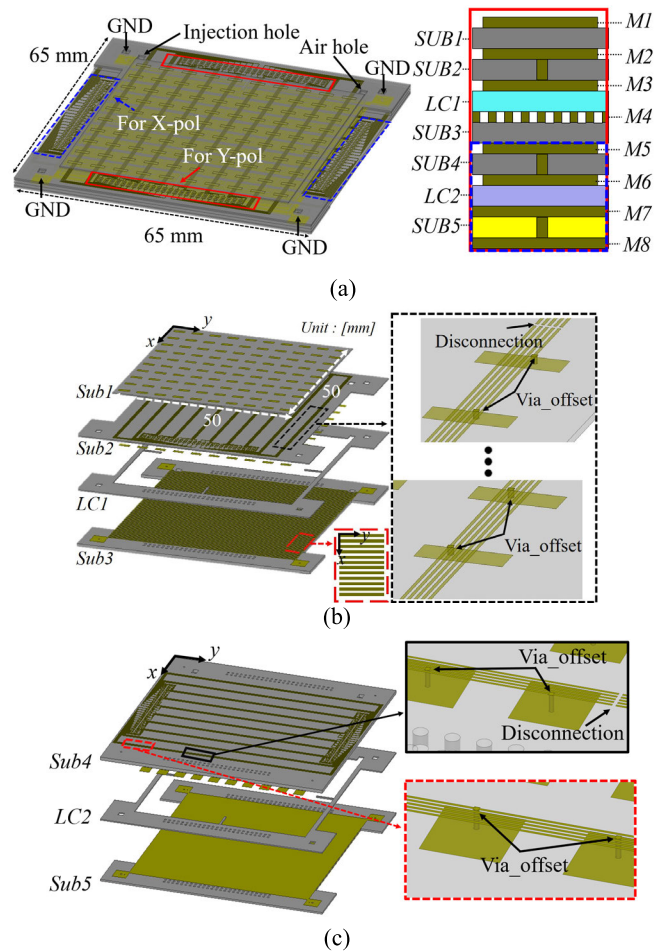Fig. 5. Magnitude responses for each polarization versus via position.

Fig. 6. (a) Entire structure of the proposed design, (b) y-polarization area (red box), and (c) x-polarization area (blue box).

the x-polarization responses, the y-polarization responses are influenced by the position in which the electric field on the rectangular patch is sensitively distorted compared with the square patch. This via effect can result in phase extraction errors when the same bias voltage is applied to all the unit cells to obtain the reflection phase.

The entire structure of the proposed RIS is shown in Fig. 6(a). The solid red and dashed blue boxes represent the

connector areas for the y- and x-polarized waves, respectively. Four common dc ground holes were selected for convenience. The holes where the 1.27-mm pitch pin headers were drilled into the bottom side of the structure. The LC injection and air holes were introduced from sub2 to the LC2 layer. Air slowly escaped from the air hole when the LC was injected into the LC hole. The size of the entire structure was 65 × 65 mm, including the radiation and additional regions. The radiation region is the area where the incoming waves are scattered and the additional region is where the bias line connected to the outer control circuit is arranged. The red and blue boxes represent the y-polarization and x-polarization areas, respectively, because the LC in the y-polarization area only manipulates the y-polarized waves.

The y-polarization area containing SUB1–SUB3 and M1–M4 is shown in Fig. 6(b). The dimensions of the radiation region were 50 × 50 mm. The via connected to each unit cell was arranged in different positions to apply a bias voltage to the unit cell. The M4 layer was introduced in the RF and dc ground for the y-polarized waves. Periodic grids were modeled as shunt inductances, operating a high-pass filter (stop responses at the target band). The gap and width of the M4 layer were 0.2 s and 0.1 mm in the case of the fabrication limit, respectively.

Fig. 7(a) and (b) depicts the top view of the two bias modules in detail. In Fig. 7(a), the bias module (y-module) responsible for controlling the y-polarized waves consists of M2, M3 metal layers, and SUB2. The M2 and M3 layers are connected through metallic via to excite the LC. The metallic vias are placed differently in each position to provide different bias signals to each LC. Moreover, the bias lines at the center were cut out to separate two sectors, each consisting of 5 × 10 cells. Consequently, the proposed RM can achieve 2-D beamforming by manipulating each unit cell. In Fig. 7(b), the bias module (x-module) responsible for controlling the x-polarized waves consists of M5, M6 metal layers, and SUB4. The bias principle of the x-module is the same as that of the y-module.

IV. MEASUREMENT RESULTS AND DISCUSSION

A. Measurement Setup and Phase Extraction

In this section, the design of the proposed LCRM is introduced, including the unit cell design, simulation results, and the entire structure of the proposed LCRM.

A photograph of the fabricated sample is shown in Fig. 8. Four holes exist for the common grounding of layers M4, M7, and M8. The connecting pin headers in the four boxes were soldered to connect the bias line to the outer control circuit. The bias lines inside the red and blue boxes correspond to the x- and y-polarized waves, respectively. Notably, the phase–voltage curves are required to manipulate the incident waves. Owing to anisotropy and inhomogeneity, the intermediate phase responses of the LC are easily extracted using this method. Phase extraction can be obtained by biasing the same voltage to all the unit cells. Subsequently, we checked the S_{21} phase on the vector network analyzer (VNA). The reflection phase of the LCRM can be obtained using a two-port VNA. An MS4647A VNA from Anritsu was used in this study.
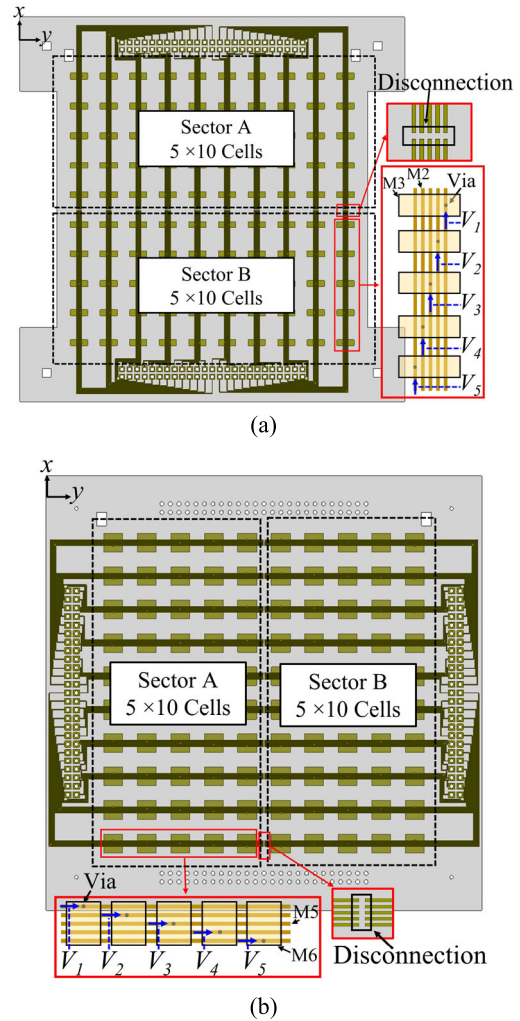

(a)

(b)

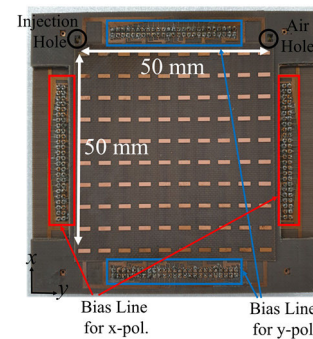Fig. 7. Top view of the two bias modules: (a) M2–SUB2–M3 and (b) M5–SUB4–M6.

Fig. 8. Photograph of the fabricated IPC-RM sample.

The Tx antenna is located at a 30° offset angle, and the focal length between the Tx and the LCRM is 4 cm. The distance between Tx and Rx antennas was set to be 60 cm. Finally, the phase difference between the phase in the non-bias state and the phase at a specific bias was calculated. The measurement setup is shown in Fig. 9(a). This setup is used for the reflectarray measurements in the following section. The LCRM was connected to two controllers, X- and Y-controllers, to control two incident waves. Phase extraction
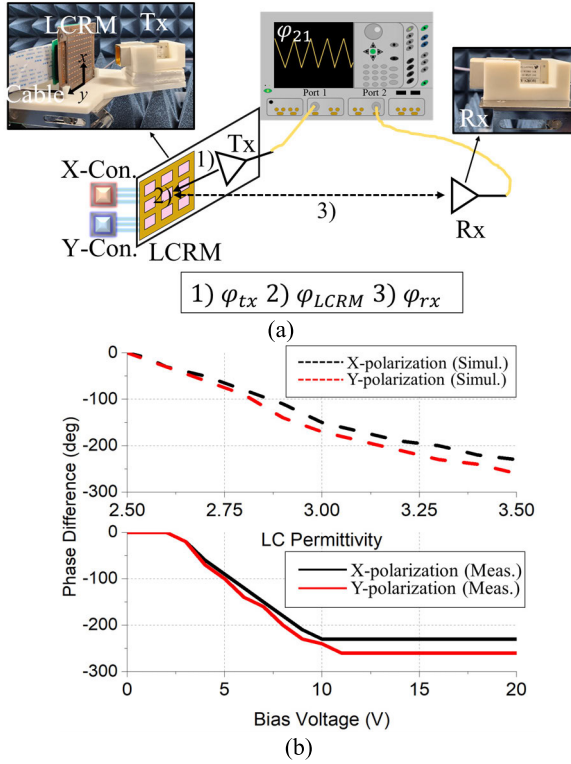
Fig. 9. (a) Measurement setup for phase–voltage curves and reflectarray and (b) simulated and measured results of phase extraction at 28 GHz.

was conducted for the x- and y-polarized cases. The Tx and Rx horn antennas used in the measurement have a gain of 13.5 dBi. The simulated and measured results of the phase extraction as a function of the LC permittivity and bias voltage are shown in Fig. 9(b). The measured results were extracted using the following:

$$\varphi_{21} = \varphi_{tx} + \varphi_{LCRM} + \varphi_{rx} \tag{10}$$

where φ_{tx} refers to the phase shift from the transmitter (Tx) horn antenna, and φ_{LCRM} represents the reflection phase shift resulting from the change in the LC in the LCRM. φ_{rx} refers to the phase shift from the LCRM to the receiver (Rx) horn antenna. The phase difference is the phase difference between the zero-bias voltage and a certain voltage that is above the Frederiks threshold voltage. The threshold voltage is 3 V.

These results are consistent with those obtained from the full-wave simulation.

B. Reflectarray Measurement

This section describes the reflectarray measurements. The reflectarray concept is shown in Fig. 1, where two polarized horn antennas simultaneously or individually feed the reflecting surface. Reflectarray measurements are relevant because antenna performance, such as aperture efficiency, beam coverage, and sidelobe level (SLL), can be validated. The measurement setup of the reflectarray was the same as that used for the phase extraction measurement.

The beamforming for the reflectarray measurement was conducted using six bias states of the unit cell, listed in Table II. The bias voltage level to control the LC is in the range of 0–11 V. Fig. 10(a) and (b) shows the phase profile

TABLE II
UNIT CELL PHASE STATE AND CORRESPONDING
BIAS LEVEL FOR THE MEASUREMENT

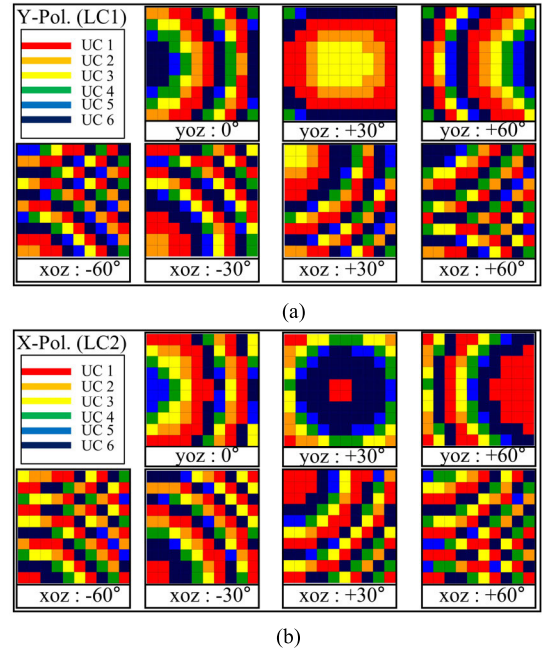| UC state #	X-pol	Y-pol
	Phase difference (°) / Bias level (V)	
UC1	0 / 0	0 / 0
UC2	-60 / 4	-70 / 4
UC3	-120 / 6	-120 / 5.5
UC4	-180 / 8	-160 / 7
UC5	-210 / 9	-210 / 8.5
UC6	-230 / 10	-260 / 11

Fig. 10. Phase profile to steer the beam for (a) y-polarization (LC1 layer) and (b) x-polarization cases (LC2 layer).

on the corresponding LC layer to achieve the desired beam patterns. Six bias states are numbered from UC1 to UC6, and those profiles were calculated using (9).

The measured E- and H-plane beam patterns are shown in Figs. 11 and 12 for each polarization case at 28 GHz, respectively. In the case of y-polarization on the xoz-plane, the measured gains and SLL were validated from 15.17 to 15.65 dBi and from −12.48 to −8.42 dB, respectively. The beam coverage range was −60° to +60°. In addition, on the yoz-plane, the measured beam patterns shown in Fig. 11(b) were 15.8–17.1 dBi. The maximum gain occurred in the yoz-plane at a steered angle of 30° because of the reduced blockage losses caused by the feed antenna and jig at the broadside.

The measured SLL results ranged from −12.4 to −6.31 dB. The beam coverage range on the yoz-plane ranged from 0° to +60°. The measured beam patterns for the x-polarized waves on the xoz-plane are shown in Fig. 12(a). The measured gain ranged from 13.05 to 15.5 dBi, and the SLL ranged from −6.78 to −15.57 dB. The beam coverage ranged from −60° to +60°. In the case of the x-polarized waves on the yoz-plane, the measured gain and SLL were 15.5–16.9 dBi and −15.8 to −4.47 dB, as shown in Fig. 12(b), respectively. The maximum
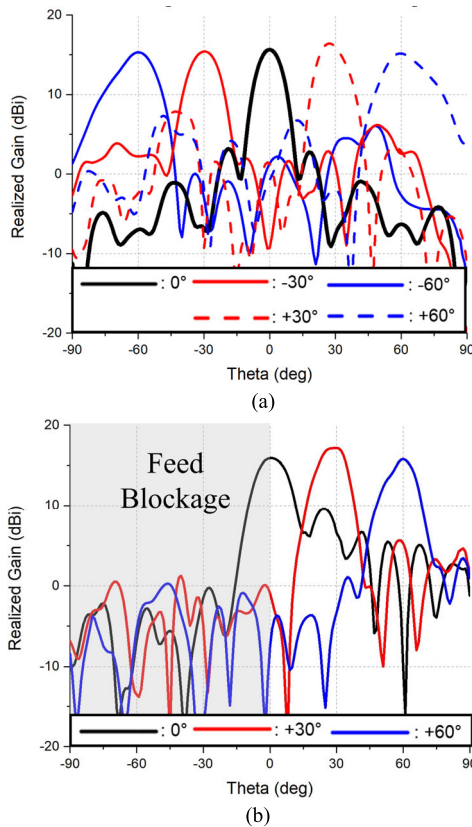
Fig. 11. Measurement beam patterns for the y-polarized waves on (a) *xoz*-plane and (b) *yoz*-plane.

Fig. 12. Measured beam patterns for the x-polarized waves on (a) *xoz*-plane and (b) yoz-plane.

steering angle in Fig. 12(b) was 60°. In summary, the beam patterns on the xoz-plane exhibited a lower gain than those on the yoz-plane. This is because the feed antenna caused blockage losses when the beam was steered in any direction on the xoz-plane at the expense of coverage. The maximum gain and the corresponding aperture efficiency were confirmed as 17.9 dBi and 22.53 %, respectively. The best gain and SLL occur at the +30° case of the x-polarization at the xoz-plane. The broadside beam patterns for the y- and x-polarized waves are shown in Fig. 13 to demonstrate the independently controllable capability of the proposed structure. When one LC layer is biased to steer the beam in the broadside direction, all the directors of another LC layer are fully biased, resulting in an extreme phase state $\varepsilon_{r\parallel}$. In that case, the metasurface operates as a reflector with a reflection loss factor. As shown in Fig. 13, the waves can be independently controlled by controlling each controller. Few dc couplings exist between the two LC layers.

This can be accomplished by the rectangular design of the metal patch above the polarizer (M4 layer) to minimize undesired polarization responses. In addition, the polarizer reflects one polarization wave, and the shunt inductance is modeled as a wave incident on the metallic layer. A performance comparison of the LCRM antennas investigated in the mmWave band is listed in Table III. This study first investigates independent polarization controllability using two LC layers. In addition, the scanning range was the highest among those of published LCRM antennas.
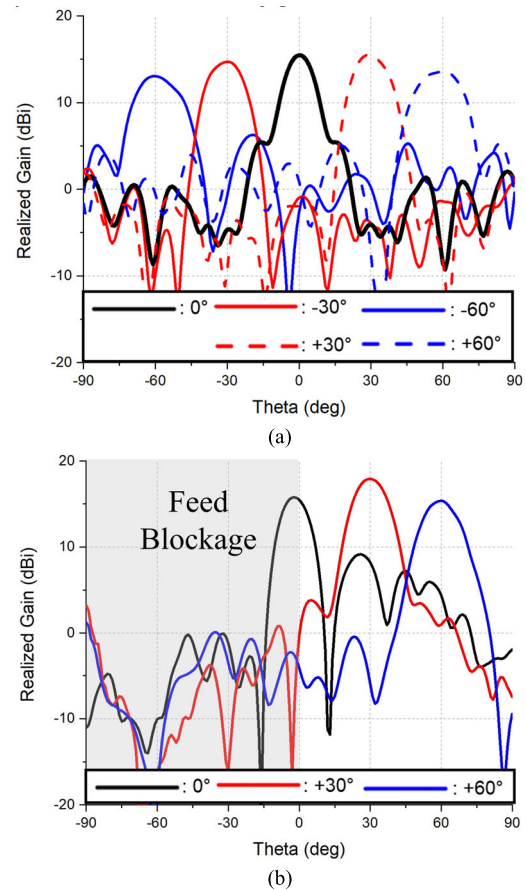
TABLE III
PERFORMANCE COMPARISON OF LCRM ANTENNAS

Feature	Ref. [23]	Ref. [8]	Ref. [24]	Ref. [20]	This work
Frequency [GHz]	100	9.55	24	24	28
Aperture Efficiency [%]	18.5	35.8	5.8	23.1	22.5
SLL [dB]	-13.0	-15.5	-	-	-15.8
Scanning Capability	1D	2D	1D	2D	2D
Scanning Range [°]	55	100	20	90	120
Independent Polarization Controllability	N.A	N.A	N.A	N.A	YES

C. Small-Aperture RIS Measurement

This section examines the RIS measurements of the proposed LCRM. The RIS concept has emerged as a key to reliable connectivity in wireless environments [25], [26], [27]. In terms of system complexity and build cost, the current wireless communication between a base station and user equipment may not be sufficient because of multipath fading, path-loss burden base station with EIRP, and spectral/energy efficiency, resulting in an increase in power consumption.

The concept of the RIS-assisted channel is shown in Fig. 1. The electromagnetic field radiating from the Tx antenna is reflected by unit cells of the RIS. The reflected fields are then received by the Rx. The RIS has several advantages, such
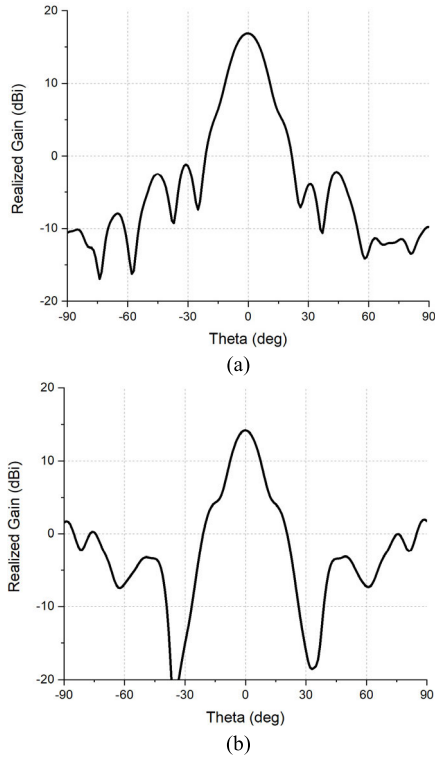
Fig. 13. Measured beam patterns for (a) y- and (b) x-polarized waves when another LC layer was fully biased.

Fig. 14. Description of the spillover efficiency when the RIS aperture is small.

as ease of deployment, efficiency enhancement, compatibility with standard topologies, and existing hardware. Although the RIS is required to be of large-scale dimension, one scenario was chosen to validate the performance of the proposed design as an RIS in this study.

Although numerous studies on RIS have been conducted, few studies have introduced RIS demonstration at 28 GHz [28]. This is because characterizing the reconfigurable components is challenging, including the varactor or p-i-n diode in the mmWave band. However, LC can be easily applied to the frequency band. In addition, common reflectarray characteristics, such as taper or spillover efficiency, have not been considered in many previous studies with RIS demonstration. Otherwise, path-loss modeling considering aperture efficiencies was introduced without practical demonstrations [29].

In this study, a small-aperture RIS test was conducted to validate the aperture efficiency, particularly the spillover efficiency, where the feed antenna solid angle coverage exceeds the physical area of the RIS, as shown in Fig. 14. Although the RIS has an electrically large dimension, spillover should be considered when the distance from the Tx to the RIS increases.

In this study, the maximum received power can be expressed using (11) from [29]

$$\frac{P_r}{P_t} = \frac{G_{Tx} \cos\theta_{tc} G_{Rx} \cos\theta_{rc} \varepsilon_{ap}^2 |\Gamma_{av}|^2 (Nd_x d_y)^2 L_{edge}}{r_{tc}^2 r_{dc}^2 (4\pi)^2} \quad (11)$$

where P_r and P_t represent the received power at the Rx and transmitted power at the Tx antenna, respectively. G_{Tx} and G_{Rx} are the gains of the Tx and Rx, respectively, whereas $\cos\theta_{tc}$
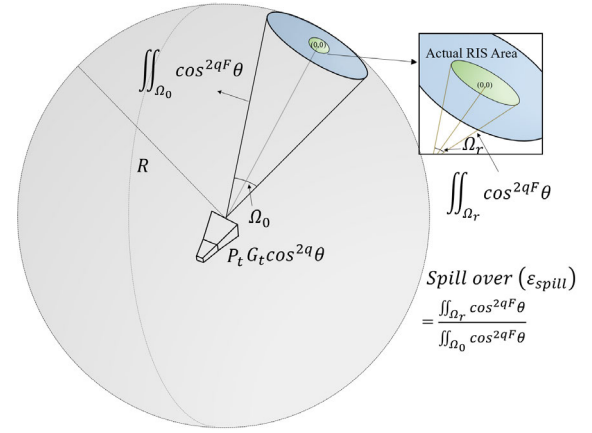
and $\cos\theta_{rc}$ are the incident and reflected angles at the center of the RIS, respectively. r_{tc} and r_{rc} denote the distance from the Tx antenna to the center of the RIS and from the center of the RIS to the Rx antenna, respectively. $|\Gamma_{av}|$ is the average loss factor after reflection by the RIS. The RIS has N unit cells, whose lateral dimension is $d_x \times d_y$, as shown in Fig. 1.

The aperture efficiency can be calculated using several methods. 1) Analytical calculation with an appropriate approximation, including the Gaussian–Legendre quadrature rule or Taylor series expansion [29]. Method (1) uses cosine modeling, where the antenna gain and roll-off pattern are defined as $(2q_F + 1)\cos^{qF}\theta$. 2) Direct field calculation using a full-wave simulation [8]. For a small aperture, diffraction from the edge of the RIS is a loss factor because the electric fields in the small RIS are slowly tapered compared with those in the large RIS. Full-wave calculations were chosen to extract ε_{ap} considering such complicated loss factors (12) and (13) [30]

$$\varepsilon_{taper} = \frac{1}{A} \frac{|\int\int_A |\overrightarrow{E_{Tx}}| \cdot |\overrightarrow{E_{cell}}||^2}{\int\int_S |\overrightarrow{E_{Tx}}|^2} \quad (12)$$

$$\varepsilon_{spillover} = \frac{\int\int_A |\overrightarrow{E_{Tx}}|^2}{\int\int_S |\overrightarrow{E_{Tx}}|^2} \quad (13)$$

where A and S denote the aperture surface of the RIS and hemisphere around the Tx antenna, respectively. The field intensities of the Tx and RIS unit cells are denoted as E_{tx} and E_{cell}. The simulated spillover and taper efficiency as a function of the distance between the Tx and RIS versus several cases of Tx antenna gain (13, 21.5, and 30 dBi) are shown in Fig. 15, according to which the higher the antenna gain, the higher the spillover efficiency. Therefore, the Tx gain for the RIS when constructing a 5G link budget should be considered. However, a high-gain antenna requires a large distance to satisfy the far-field distance and low taper efficiency requirements [31].

The measurement setup of the proposed design as an RIS is shown in Fig. 16. The Tx antenna was connected to a vector signal generator (SMW200A, Rohde & Schwarz), and the Rx antenna was connected to a spectrum analyzer (MS2760A, Anritsu). A 28-GHz continuous wave from the signal generator
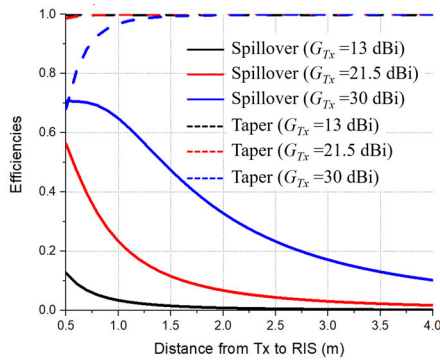
Fig. 15. Calculated spillover and taper efficiency as a function of the distance between Tx and RIS versus Tx antenna gain.
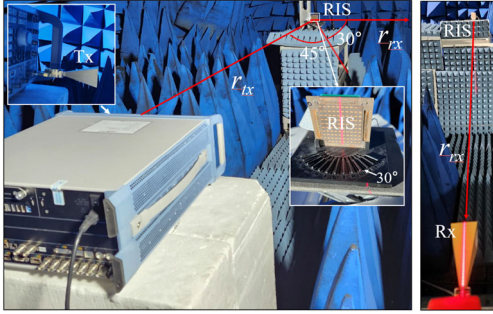

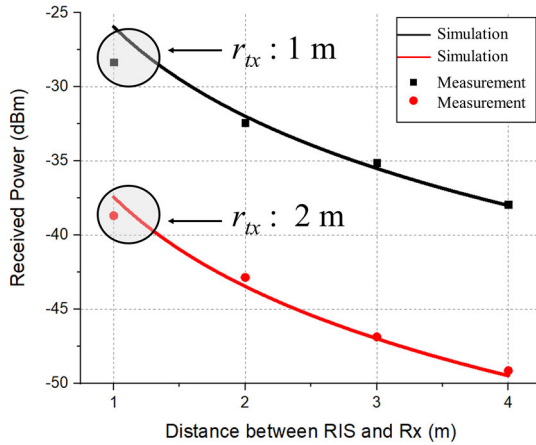Fig. 16. Measurement setup of the proposed design as an RIS.

Fig. 17. Measurement results of the small-aperture RIS.

was transmitted to the RIS at an angle of incidence of 45°. Subsequently, the RIS reflected the signal toward Rx at an angle of 30°. Finally, the received power was extracted using a laptop. Because the path-loss modeling was based on the far-field wave, the minimum distance at which the wave travels to the TEM was calculated to be 1 m. The input power, Tx, and Rx antenna gains were 20 dBm, 21.5 dBi, and 21.5 dBi, respectively.

The measurement results for the small-aperture RIS are shown in Fig. 17. The points were extracted by averaging the ripple data from the received power; the ripple was 1–2 dB at each point. Owing to the small aperture, the difference between the received powers for the two cases (1 and 2 m of r_{tx}) was above 6 dB, and such differences mainly originate

from spillover efficiency. The error at a distance of 1 m between the RIS and the Rx was higher than at other distances because of the non-line-of-sight gain between the Tx and Rx antennas, unit cell diffusion, and edge diffraction.

V. CONCLUSION

This study first introduced an independent polarization-controllable structure for an LC-based RMS in the mmWave band. The proposed structure can be used for a reflectarray antenna or RIS. In reflectarray applications, the aperture efficiency, SLL, and beam scanning range were demonstrated. In the RIS test, the small-aperture RIS concept was demonstrated and the received power followed the Friis equation and also decreased proportionally to the square of the distance. Although path-loss modeling, considering spillover and taper efficiencies, has been previously investigated, the demonstration of a small aperture was first introduced in this study. The proposed structure and RIS scenario are promising for future studies on LC-based reflectarrays or small-aperture RIS.

REFERENCES

[1] Y. Youn, J. Choi, B. Kim, W. Hwang, C.-Y.-D. Sim, and W. Hong, "Dual-band patch antenna matching network comprised of separated ground layers and via posts for adjustable return current path," *IEEE Access*, vol. 10, pp. 102173–102180, 2022.

[2] J. Seo et al., "Miniaturized dual-band broadside/endfire antenna-in-package for 5G smartphone," *IEEE Trans. Antennas Propag.*, vol. 69, no. 12, pp. 8100–8114, Dec. 2021.

[3] G. S. Karthikeya, S. K. Koul, A. K. Poddar, and U. L. Rohde, "Compact bent-corner orthogonal beam switching antenna module for 5G mobile devices," *J. Electromagn. Eng. Sci.*, vol. 22, no. 1, pp. 74–83, Jan. 2022.

[4] J. Oh, B. Kim, S. Yoon, K. Kim, E. J. Sung, and J. Oh, "High-gain millimeter-wave antenna-in-display using non-optical space for 5G smartphones," *IEEE Trans. Antennas Propag.*, vol. 71, no. 2, pp. 1458–1468, Feb. 2023.

[5] S. Kim and S. Nam, "Design of a relocatable antenna element module for a Ku-band reconfigurable array with low mutual coupling," *J. Electromagn. Eng. Sci.*, vol. 22, no. 4, pp. 534–536, Jul. 2022.

[6] Y. Kim, H. Kim, I. Yoon, and J. Oh, "4 × 8 patch array-fed FR4-based transmit array antennas for affordable and reliable 5G beam steering," *IEEE Access*, vol. 7, pp. 88881–88893, 2019.

[7] S. D. Targonski, D. M. Pozar, and H. D. Syrigos, "Analysis and design of millimeter wave microstrip reflectarrays," in *IEEE Antennas Propag. Soc. Int. Symp. Dig.*, vol. 1, Jun. 1995, pp. 287–296.

[8] H. Kim, J. Kim, and J. Oh, "Communication a novel systematic design of high-aperture-efficiency 2D beam-scanning liquid-crystal embedded reflectarray antenna for 6G FR3 and radar applications," *IEEE Trans. Antennas Propag.*, vol. 70, no. 11, pp. 11194–11198, Nov. 2022.

[9] S. Lee, Y. Nam, Y. Kim, J. Kim, and J. Lee, "A wide-angle and high-efficiency reconfigurable reflectarray antenna based on a miniaturized radiating element," *IEEE Access*, vol. 10, pp. 103223–103229, 2022.

[10] I. Nam, S. Lee, and D. Kim, "Miniaturized beam reconfigurable reflectarray antenna with wide 3-D beam coverage," *IEEE Trans. Antennas Propag.*, vol. 70, no. 4, pp. 2613–2622, Apr. 2022.

[11] H. Kim, J. Kim, and J. Oh, "Liquid-crystal-based X-band reactively loaded reflectarray unit cell to reduce reflection loss," *IEEE Antennas Wireless Propag. Lett.*, vol. 20, no. 10, pp. 1898–1902, Oct. 2021.

[12] R. Kowerdziej, J. Wróbel, and P. Kula, "Ultrafast electrical switching of nanostructured metadevice with dual-frequency liquid crystal," *Sci. Rep.*, vol. 9, no. 1, p. 20367, Dec. 2019.

[13] M. W. Geis, T. M. Lyszczarz, R. M. Osgood, and B. R. Kimball, "30 to 50 ns liquid-crystal optical switches," *Opt. Exp.*, vol. 18, no. 18, pp. 18886–18893, 2010.

[14] D. C. Zografopoulos and R. Beccherelli, "Tunable terahertz fishnet metamaterials based on thin nematic liquid crystal layers for fast switching," *Sci. Rep.*, vol. 5, no. 1, p. 13137, Aug. 2015.

[15] S. Bildik, S. Dieter, C. Fritzsch, W. Menzel, and R. Jakoby, "Reconfigurable folded reflectarray antenna based upon liquid crystal technology," *IEEE Trans. Antennas Propag.*, vol. 63, no. 1, pp. 122–132, Jan. 2015.

[16] G. Perez-Palomino et al., "Design and experimental validation of liquid crystal-based reconfigurable reflectarray elements with improved bandwidth in F-band," *IEEE Trans. Antennas Propag.*, vol. 61, no. 4, pp. 1704–1713, Apr. 2013.

[17] E. Doumanis et al., "Nematic liquid crystals for reconfigurable millimeter wavelength antenna technology," in *Proc. 7th Eur. Conf. Antennas Propag. (EuCAP)*, Apr. 2013, pp. 1791–1792.

[18] P. G. de Gennes and J. Prost, *The Physics of Liquid Crystals*. Oxford, U.K.: Clarendon, 1995.

[19] G. Perez-Palomino et al., "Accurate and efficient modeling to calculate the voltage dependence of liquid crystal-based reflectarray cells," *IEEE Trans. Antennas Propag.*, vol. 62, no. 5, pp. 2659–2668, May 2014.

[20] X. Li et al., "Broadband electronically scanned reflectarray antenna with liquid crystals," *IEEE Antennas Wireless Propag. Lett.*, vol. 20, no. 3, pp. 396–400, Mar. 2021.

[21] J. Yang et al., "Fully electronically phase modulation of millimeter-wave via comb electrodes and liquid crystal," *IEEE Antennas Wireless Propag. Lett.*, vol. 20, no. 3, pp. 342–345, Mar. 2021.

[22] N. Marcuvitz, Ed., *Waveguide Handbook* (IEE Electromagnetic Waves Series 21). New York, NY, USA: McGraw-Hill, 1951, pp. 218–280.

[23] G. Perez-Palomino et al., "Design and demonstration of an electronically scanned reflectarray antenna at 100 GHz using multiresonant cells based on liquid crystals," *IEEE Trans. Antennas Propag.*, vol. 63, no. 8, pp. 3722–3727, Aug. 2015.

[24] W. Zhang, Y. Li, and Z. Zhang, "A reconfigurable reflectarray antenna with an 8 μm-thick layer of liquid crystal," *IEEE Trans. Antennas Propag.*, vol. 70, no. 4, pp. 2770–2778, Apr. 2022.

[25] Ö. Özdogan, E. Björnson, and E. G. Larsson, "Intelligent reflecting surfaces: Physics, propagation, and pathloss modeling," *IEEE Wireless Commun. Lett.*, vol. 9, no. 5, pp. 581–585, May 2020.

[26] Y. Liu and C. D. Sarris, "Efficient propagation modeling for communication channels with reconfigurable intelligent surfaces," *IEEE Antennas Wireless Propag. Lett.*, vol. 21, no. 10, pp. 2120–2124, Oct. 2022.

[27] M. A. ElMossallamy, H. Zhang, L. Song, K. G. Seddik, Z. Han, and G. Y. Li, "Reconfigurable intelligent surfaces for wireless communications: Principles, challenges, and opportunities," *IEEE Trans. Cognit. Commun. Netw.*, vol. 6, no. 3, pp. 990–1002, Sep. 2020.

[28] J. Jeong, J. H. Oh, S. Y. Lee, Y. Park, and S. Wi, "An improved path-loss model for reconfigurable-intelligent-surface-aided wireless communications and experimental validation," *IEEE Access*, vol. 10, pp. 98065–98078, 2022.

[29] S.-K. Chou, O. Yurduseven, H. Q. Ngo, and M. Matthaiou, "On the aperture efficiency of intelligent reflecting surfaces," *IEEE Wireless Commun. Lett.*, vol. 10, no. 3, pp. 599–603, Mar. 2021.

[30] A. Z. Elsherbeni, P. Nayeri, and F. Yang, *Reflectarray Antennas: Theory, Designs, and Applications*. Hoboken, NJ, USA: Wiley, 2018.

[31] W. L. Stutzman and G. A. Thiele, *Antenna Theory and Design*. Hoboken, NJ, USA: Wiley, 2012.

Seungwoo Bang (Graduate Student Member, IEEE) received the B.S. degree from the Seoul National University of Science and Technology, Seoul, South Korea, in 2022. He is currently pursuing the integrated master's and Ph.D. degrees with the Department of Electrical and Computer Engineering, Seoul National University, Seoul.

His current research interests include metasurface and antenna design.

Hyunjun Yang (Graduate Student Member, IEEE) received the B.S. degree in electronic and electrical engineering from the Pohang University of Science and Technology (POSTECH), Pohang, South Korea, in 2020. He is currently pursuing the integrated master's and Ph.D. degrees with the Department of Electrical Engineering and Computer Science, Seoul National University, Seoul, South Korea.

His current research interests include ray tracing EM analysis technique, EM theory, wireless propagation channel measurement and modeling, and reconfigurable intelligent surface (RIS).

Byeongjin Kim (Graduate Student Member, IEEE) received the B.S. degree in electrical and computer engineering from Seoul National University, Seoul, South Korea, in 2020, where he is currently pursuing the integrated master's and Ph.D. degrees.

His current research interests include display antenna and metasurface antenna for 5G millimeter-wave communication systems.

Hogyeom Kim (Graduate Student Member, IEEE) received the B.S. degree in electrical engineering from Inha University, Incheon, South Korea, in 2016. He is currently pursuing the integrated master's and Ph.D. degrees with Seoul National University, Seoul, South Korea.

He served in the Korea Army from 2016 to 2018. His current research interests include transmit/reflectarray antennas, reconfigurable intelligence surfaces for B5G/6G communication, and millimeter-wave radar systems. Also, liquid-crystal material-based metasurface is one of the research topics.

Seongwoog Oh (Graduate Student Member, IEEE) received the B.S. degree in electrical engineering and computer science from the Gwangju Institute of Science and Technology College, Gwangju, South Korea, in 2016, and the M.S. degree in electrical engineering from Seoul National University, Seoul, South Korea, in 2018, where he is currently pursuing the Ph.D. degree in electrical engineering.

His current research interests concerned the design of microwave integrated circuits, antenna-on-package systems for 5G/6G communication, and microwave brain stimulation.

Jungsuek Oh (Senior Member, IEEE) received the B.S. and M.S. degrees from Seoul National University, Seoul, South Korea, in 2002 and 2007, respectively, and the Ph.D. degree from the University of Michigan, Ann Arbor, MI, USA, in 2012.

From 2007 to 2008, he was with Korea Telecom as a Hardware Research Engineer, working on the development of flexible RF devices. In 2012, he was a Post-Doctoral Research Fellow with the Radiation Laboratory, University of Michigan. From 2013 to 2014, he was a Staff RF Engineer with Samsung Research America, Dallas, TX, USA, working as a Project Leader for the 5G/millimeter-wave antenna system. From 2015 to 2018, he was a Faculty Member with the Department of Electronic Engineering, Inha University, Incheon, South Korea. He is currently an Assistant Professor with the School of Electrical and Computer Engineering, Seoul National University. He has published more than 40 technical journal and conference papers. His research areas include mmWave beam focusing/shaping techniques, antenna miniaturization for integrated systems, and radio propagation modeling for indoor scenarios.

Dr. Oh is the recipient of the 2011 Rackham Predoctoral Fellowship Award from the University of Michigan. He has served as a Technical Reviewer for IEEE TRANSACTIONS ON ANTENNAS AND PROPAGATION and IEEE ANTENNA AND WIRELESS PROPAGATION LETTERS, among other journals. He has served as a TPC Member and as a Session Chair for the IEEE AP-S/USNC-URSI and ISAP.